Advanced Powder Technology 20 (2009) 234–239

Contents lists available at ScienceDirect

Advanced Powder Technology

journal homepage: www.elsevier.com/locate/apt

Original Research Paper

# Measurement of electrostatic dipoles and net charge on particles suspended in air

Payel Bagga [a], John Abrahamson [a,*], John Marshall [b]

[a] Chemical and Process Engineering Department, University of Canterbury, Private Bag 4800, Christchurch, New Zealand
[b] SETI Institute, 515 N Whisman Rd., Mountain View, CA, USA

ARTICLE INFO

*Article history:*
Received 17 March 2009
Accepted 17 March 2009

*Keywords:*
Particles
Electrostatic
Dipoles
Measurement
Tribocharging

ABSTRACT

Explanations of electrostatic behaviour of individual particulates have always invoked *net* electrostatic charge and neglected any fixed dipoles arising from nonuniform distribution of charge on their surface. Here for the first time, techniques are described to measure both net charge of each particle and its dipole moment by sampling, photography, and movement analysis of particles suspended in air. In this study, spherical dielectric particles were subjected to a non-uniform electric field (around a probe) and their trajectory was followed with a multi-flash high-speed video camera. These first results support the existence of fixed or "permanent" dipoles, on tribocharged particles.



## 1. Introduction

The electrostatic behaviour of dust affects phenomena such as dust storms and dust devils on Earth and Mars [1], volcanic plumes [2,3], and planetary formation from a nebula [4], while in industry, pneumatic conveying and fluidized beds often create strong electrostatic forces on particles. These forces are used in applications such as photocopying, printing, powder coating, air conditioning and filtering, and electrostatic separation and beneficiation. Importantly, electrostatic forces appear to determine drug or toxic particle retention in the lung after inhalation [5]. Abrahamson and Marshall [6] proposed that "permanent electric dipoles" can be created on dielectric particles, producing high attractive forces in some circumstances (in dense clouds for example). These dipoles are expected to be present in many particle systems and can account for stronger particle interactions than predicted by the effects of net charge alone. Dipole forces between particles act at closer range than net charge forces, and are expected to be cumulative in a dust aggregating environment, and thus grow as the particles aggregate (experimental observations by Marshall et al. [7]), rather than mutually cancelling as generally happens in systems dominated by net charge. Prior to the 2002 paper, little attention had been given to electrostatic dipoles after the theoretical work of Zebel [8].

Dipoles are expected to often dramatically enhance the mutual collision rate of diffusing particles (adding to the effects of Brownian or turbulent motion). The discussion of this in Abrahamson and Marshall [6] has been used by astrophysicists [9] to explain the particle aggregation rates necessary to allow planets to form. However, this spreading awareness of the possible influence of discrete dipoles on particle behaviour is still based largely on theory, with the exception of some microgravity experiments [3]. Individual particle dipoles have still not yet been measured in practical situations.

This paper is concerned with the combined measurement of monopole (net) charge and dipole moment on individual particles in a cloud of dielectric particles soon after dispersion in air. This work is a first step towards better understanding of charge distributions over the surface of particles, and relating this to their collision history. The measurements were enabled by fast video and synchronized illumination and image analysis techniques. The key aspect of our method is the observation of particles passing through a non-uniform electric field, where at high gradients of field, forces due to a dipole moment are expected to dominate over forces due to net charge. By fitting particle trajectories through various parts of the field, these electrical effects can be separately assessed.

## 2. Experimental method and apparatus

A simple wire probe immersed in the suspension flow was chosen as the most convenient way to generate a non-uniform field. Application of high voltage to this probe provided a nearly spherical field around and in front of the tip of the probe. This voltage was reversed in polarity frequently during a run, to allow a symmetrical treatment of both positive and negative particles while flows and velocities remain constant (reducing possible distribution bias), and also to provide additional checks on the trajectory

* Corresponding author. Tel.: +64 3 3642318; fax: +64 3 3642063.
*E-mail addresses:* payelbagga78@yahoo.com (P. Bagga), john.abrahamson@canterbury.ac.nz (J. Abrahamson), jmarshall@seti.org (J. Marshall).

0921-8831/$ - see front matter © 2009 The Society of Powder Technology Japan. Published by Elsevier BV and The Society of Powder Technology Japan. All rights reserved.
doi:10.1016/j.apt.2009.03.002

analysis when a polarity switch occurred during a trajectory. One expects that the charge parameters of a particle will remain constant before and after such switches. For most runs the direction of any dipoles was preset before particles moved close to the probe, by subjecting them to a constant transverse field between two plates. Also this field removed some particles with higher net-charge, to allow easier analysis of the dipoles present.

A dilute flow ($5 \times 10^{-4}$ volume fraction) of spherical dielectric particles was continuously supplied by an air jet from a brush feeder. This suspension emerged from a small tube into a much larger tube along its axis, and after passing between the pre-selector plates, flowed around the probe (which pointed upstream). Close to the probe, video images were taken of particle trajectories. Multiple images were possible through the use of multiple laser flashes for each video frame, leading to a sequence of particle positions along the trajectory within each frame. Fig. 1 depicts a flow schematic of the experimental system, showing the relationship between the sampler unit, laser, high-speed camera, and the high-voltage power supply.

### 2.1. Sampler unit

The sampler unit was built around a cylindrical stainless steel tube of 100 mm ID and 500 mm length, aligned horizontally. The geometry of this sampler unit is shown in Figs. 2 and 3. This tube acted both as the outer (earthed) electrode and the channel for the particle/air suspension flow. The particles were blown off a nylon brush through a brass tube 10 mm ID and 25 mm length, leading into a polyacetal tube of 3 mm ID and 90 mm length. The polyacetal tube tip was 220 mm upstream of the probe. The probe was a fine tungsten wire of 500 μm diameter with a hemispherical tip and was mounted midway along the tube on its centreline. The wire was attached to a high-voltage supply.

The pre-selection vertical plates were 50 mm wide and 150 mm long, each 5 mm from the centreline, and 30 mm upstream of the probe. One plate was attached to a −10 kV DC supply and the other to earth.

### 2.2. Laser unit and high-voltage supply for probe

The red laser (Roithner Lasertechnik, Austria, RLT67300T, 670 nm) was rated at 300 mW of continuous optical output, and was pulsed at 200 mW power level. After enlarging the cylindrical beam with a diverging–converging lens arrangement, it was expanded into a rectangular sheet of $10 \times 0.8$ mm cross-section.

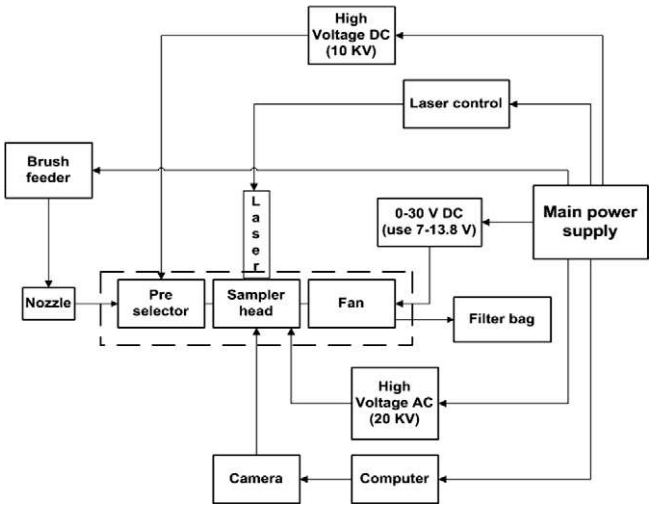


**Fig. 1.** Flow diagram of the experimental apparatus.

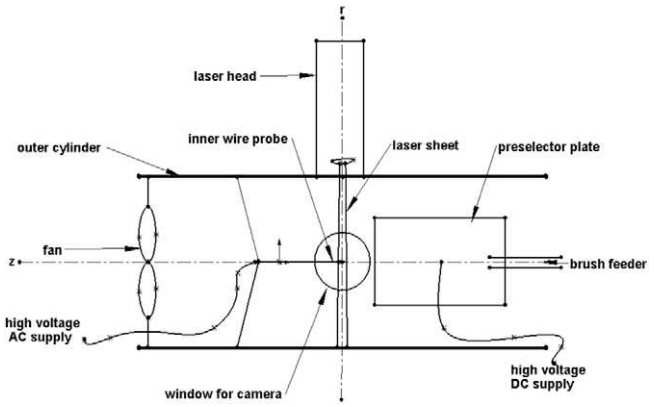


**Fig. 2.** Sectional view of the sampling unit arrangement in the plane of the laser sheet and perpendicular to the camera axis.

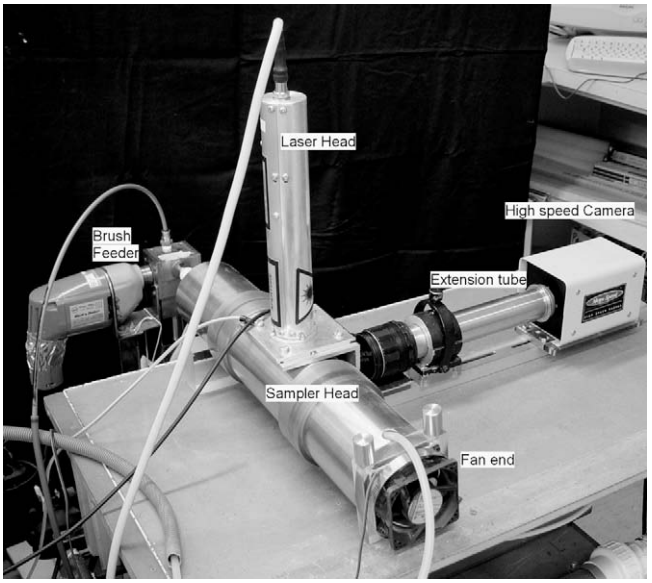


**Fig. 3.** Photograph of the sampling head, including the mounted camera, laser and electrical connections.

The laser driver controlled pulse duration, pulse-to-pulse period and the number of flashes per frame (up to 33). The laser head was mounted on the sampler tube with the sheet in line with the tip of the probe to illuminate particles close to the probe in a plane perpendicular to the axis of the video camera. The camera triggered the laser at the start of capture.

The high-voltage supply abruptly changed the polarity of the probe voltage after a set number of video frames and its square wave form had a maximum of 40 kV peak to peak. In order to indicate which polarity existed during the exposure of a video frame, the supply waveform was sent to the laser driver, which halved the frequency of pulsing when the output voltage was positive.

### 2.3. High speed camera

The CMOS high speed camera (Canadian Photonics Lab MS50K) was operated at 489 frames/s with a resolution of $1200 \times 1020$ pixels. A field of view of 6.5 mm by 5.5 mm could be imaged through the 85 mm lens on a 230 mm extension tube. Depth of field was 0.85 mm. The camera imaged through a flat glass window on the side of the tube.

### 2.4. Test particles

These were multidisperse borosilicate glass bubbles supplied by 3 M (K15 Scotchlite) sized 4–100 μm with a mean size of 37 μm. 3 M listed the particle density as 150 kg/m$^3$, indicating that the glass wall thickness was less than 1% of the diameter. Glass bubbles rather then solid spheres were chosen for rapid orientation of permanent dipoles (having low rotational inertia) and to minimize induced dipoles (having low bulk polarisable mass).

## 3. Theoretical model

The rate of change of particle velocity was calculated through particle momentum conservation as in Eq. (1), using drag force, $F_d$, and electrical force, $F_{el}$, as the dominant forces acting,

$$m\frac{d\vec{U_p}}{dt} = \vec{F_d} + \vec{F_{el}} \tag{1}$$

where $m$ is the mass of the particle. This vector equation was applied in both $z$ and $r$ directions, (neglecting gravitational force). The $F_d$ direction opposed $U_{rel}$ and the magnitude obtained via the drag coefficient correlation proposed by Abraham [10]. This drag force was resolved in the $z$ and $r$ directions and components inserted in the corresponding $z$ and $r$ momentum equations.

The flow field around the hemispherical tip was taken as that approaching a sphere, using Stokes' equations [11]. The relevant angles and points used are shown in Fig. 4.

The electrostatic force was taken as the sum of the monopole, dipolar, induced dipole and the image forces.

$$\vec{F_{el}} = \vec{F}_{mono} + \vec{F}_{dip} + \vec{F}_{ind} + \vec{F}_{image} \tag{2}$$

All of these act along the probe centre-to-particle centre direction, and are a function of their separation $r_{sph}$. Thus

$$F_{el} = \frac{Q_{net}V}{(1/a-1/b)r_{sph}^2} + \frac{-2PV}{(1/a-1/b)r_{sph}^3} + U\frac{-8\pi\varepsilon_o V^2 R_p^3}{(1/a-1/b)^2 r_{sph}^5} + \frac{-Q_{net}^2}{16\pi\varepsilon_o(r_{sph}-a)^2} + \frac{-Q_{dip}^2}{16\pi\varepsilon_o(r_{sph}-R_p-a)^2} \tag{3}$$

where $a$ is probe tip radius, $b$ is tube radius, $Q_{dip} = P/2R_p$, $P$ is dipole strength, $V$ is probe voltage, $R_p$ is particle radius, $U$ is the permittivity multiplication factor [12], $Q_{net}$ is the net charge, and $\varepsilon_o$ is free space permittivity.

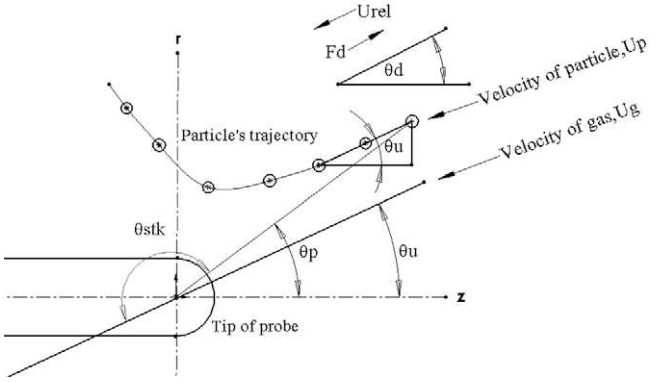


**Fig. 4.** Relevant angles and points used for modelling particle trajectories around a high-voltage probe pointing upstream. ($\theta_u$ and $\theta_p$ are the angles of gas velocity and particle position, $\theta_d$ is the angle of drag force and relative velocity $U_{rel} = U_p - U_g$, all relative to the $z$ axis and $\theta_{stk}$ is the Stokes angle, particle position angle relative to the gas approach axis.).

### 3.1. Rotation of particles

Rotation of the particle in the electric field is driven by the torque acting on the dipole, and was calculated assuming that the dipole charges do not move along the particle surface. The angular acceleration of the particle was calculated from the angular momentum conservation equation, using the component of local field which is perpendicular to the dipole, acting on the dipole to provide turning torque, and using a viscous drag torque to resist. Appendix A gives details of the treatment. The major angle to note is the dipole-to-field angle (see Fig. A.2 ), taken as 90° at the start of analysis (dipole pointing out of page in Fig. A.1) when the preselector plates were used.

### 3.2. Fitting particle trajectories

Owing to the transparency of the glass bubbles, sensing their position depended on being able to record side-scattered light from the laser sheet. Thus, only the tops and bottoms of particles were visible (via small light patches). The centre of a particle was taken to be the midpoint between the farthest pixels of each pair of light patches.

The $r$ and $z$ versions of Eq. (1) were integrated in Excel spreadsheets to predict particle positions $r$ and $z$ at time intervals much smaller than the flash-to-flash period. Those $r$ and $z$ for flash times were then fitted to the photographic $r$ and $z$ by adjustment of net charge and dipole moment values in the electrical force expressions. Estimation of drag force presumed knowledge of the gas velocity and direction. For each trajectory, the initial velocity (magnitude and direction) of the *particle* while entering the field of view was assumed to be that of the *gas* during the whole trajectory.

Fig. 4 shows schematically a typical particle trajectory bending away from the probe, with axes, velocities, and various angles used in the analysis. The probe tip centre was considered as the origin for both radial and axial positions in cylindrical co-ordinates.

The procedure used for fitting the integrated distances to experimental distances was as follows

1. The first few particle positions on the frame were used to calculate the radial and axial velocities of the particle, and assumed to be those of the gas, giving the velocity and angle of gas approach to the probe (assumed constant).
2. The net charge $Q_{net}$ on the particle was varied to fit the model to points closer to the tip of the probe.
3. Dipole moment $P$ was varied together with some minor adjustment of monopole charge to fit points even closer to the probe.

Image forces were calculated by adding contributions (a) due to the fitted monopole charge with minimum separation distance equal to the radius of the particle, and (b) due to the fitted (closer) dipole charge ($P$/ particle dia) with minimum separation distance of 10 μm (roughness on probe surface).

## 4. Results

Fig. 5 shows a frame captured with the high-speed video camera. For all measurements reported here the pulse-to-pulse interval was kept at 160 μs with pulse duration of 20 μs and camera capture rate 489/s. A good fit meant that predicted points agreed with image points both in trajectory path and distance along the path.

The parameters used in numerical calculations were tip radius $a = 2.5 \times 10^{-4}$ m, tube inner radius $b = 0.05$ m, apparent density of the glass bubbles $\rho_p = 150$ kg/ m$^3$, permittivity of free space $\varepsilon_o = 8.85 \times 10^{-12}$ F/m, multiplication factor for the glass bubbles $U = 0.0195$, and viscosity of air $\mu = 1.8 \times 10^{-5}$ Pa s.

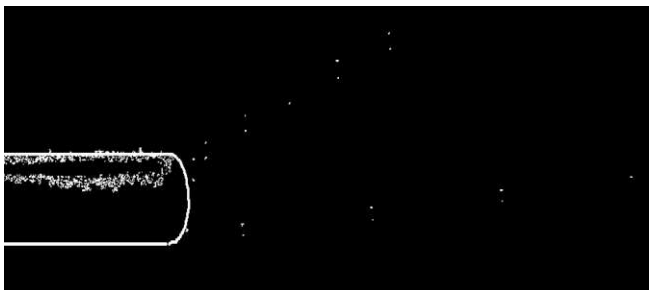

**Fig. 5.** Composite image (from two frames) of two of particles and the probe as captured with the camera.

The four trajectories presented here are typical of many analyzed, but these are the first results of the technique and distributions of net charge and dipole strength have not yet been obtained. The analysis is manual and laborious at this point, but will be automated. Figs. 6 and 7 show two examples with fitted dipole charges exceeding the fitted net charge. In contrast, the two examples in Fig. 8 indicate that no apparent dipole is present, and net charges are sufficient to explain each path. Error bars are for 1 pixel image error in both directions.

Fig. 6 shows modelled and observed trajectories of an 80 μm particle, for a probe voltage of −6 kV. Assuming solely net charge gave wide deviation close to the tip of the probe. The addition of a dipole gave a good fit up to the probe. Fitting errors were determined by adjustment of both dipole moment and net charge so that the modelled trajectories just remained within the experimental error bars. This resulted in errors of $\pm 0.5 \times 10^{-14}$ C for the net charge (i.e. around 10%) and $\pm 2.5 \times 10^{-14}$ C for the dipole charge (also about 10%). The model indicated ranges of $r_{sph}$ over which net charge, dipole and image forces were dominant, as follows: 3600 μm > net charge > 600 μm > dipole > 300 μm > image charge > contact point (260 μm).

Fig. 7 shows similar trajectories of a 60 μm particle at a probe voltage of −7 kV. The prediction indicates that the particle has touched the probe between the last two images. The last position captured by the camera is then after rebound from the probe (dotted line).

Fig. 8 shows the trajectories of two particles that fitted well for net charge and zero dipole moment (within error of $1.5 \times 10^{-14}$ C dipole charge). As in Fig. 7, there is some discrepancy when fitting the last point presumably due to particle movement after reaching the surface.

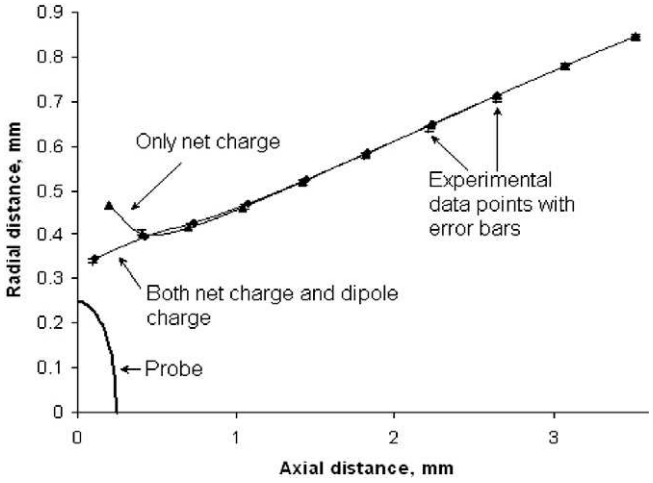


**Fig. 6.** Experimental and model trajectories for an 80 μm particle at probe voltage −6 kV. For only net charge fitted the charge is $q_{net} = -4 \times 10^{-14}$ C and for both net charge and dipolar charge fitted the values are $q_{net} = -7.5 \times 10^{-14}$ C and $q_{dip} = 2.7 \times 10^{-13}$ C.

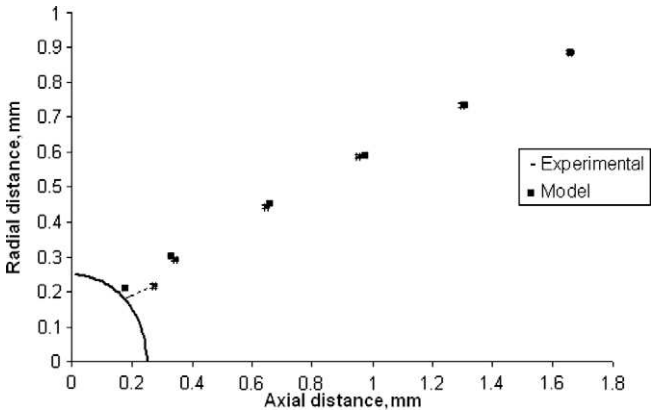


**Fig. 7.** Experimental 60 μm particle trajectory at −7 kV compared with model predictions. The fitted net charge $q_{net} = -2.5 \times 10^{-14}$ C and dipolar charge $q_{dip} = 2 \times 10^{-13}$ C.

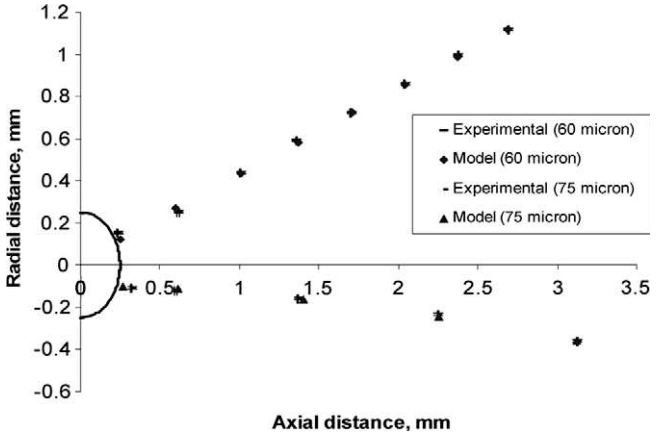


**Fig. 8.** Experimental and predicted particle trajectories for a 60 μm particle with probe voltage −6 kV with fitted net charge $q_{net} = +3.9 \times 10^{-14}$ C and a 75 μm particle with probe voltage −10 kV with fitted net charge $q_{net} = -4.4 \times 10^{-14}$ C.

## 5. Discussion

This paper covers only "proof of concept" exploratory measurements, with little attention given to (tribo)charging conditions for the particles. However, it can be seen from the results above that both the net charge and the dipole moment values were statistically significant, and so the measurement technique appears to be successful.

The experiments examined the particles in the plume from a relatively high velocity jet where significant turbulence is expected (jet velocity 35 m/s), with expected turbulent velocities of around 10 m/s and integral length scales $\Lambda$ of around 10 mm near the probe [13]. It is thus to be expected that initial particle velocities varied somewhat in direction, as observed. Most of the turbulent energy is contained in eddies much larger than $\Lambda$. Trajectories within the experimental view span (3 or 4 mm) are easily within the high energy eddy size and are thus expected to have only a slowly changing gas velocity, supporting the assumption made that it is constant over the length of a trajectory. Thus the tech-

nique appears to cope with turbulence larger than that expected in most industrial and natural situations.

The "dipole charge" values reported here are a *minimum*, derived from the fitted dipole moment by using the maximum separation distance (particle diameter). In reality, with charge expected to be distributed randomly around each particle surface in patches [6], most dipole charge separations will be smaller. It is interesting that for some particles sampled in this study, this minimum charge for the dipole was much larger than the net charge.

The rotation calculation treated in Appendix A showed small rotation times for the fields used in this work. For example for the particle described in Fig. 6 the rotation time of the dipole to orient in the direction of electric field was close to 340 μs. On a particular frame this is the time taken between two consecutive images of particle in a trajectory.

This technique opens up the possibility of measurement of the distribution of permanent dipoles on dust and grit in both natural events and in industry. These distributions relate to the conditions of tribocharging (collisions among particles and with walls), and it is expected that (a) tribocharging will be understood more deeply, and (b) consequent behaviour may be predicted, such as the aggregation rates of clouds of particles, their effective diffusivity and effective viscosity as an ensemble (e.g. in a fluid bed, or in a freely flowing granular bed).

## 6. Conclusions

A new technique for measuring electrical dipoles on suspended particles has been described. It appears to have adequate sensitivity to show the existence and importance of dipoles on tribocharged particles. It is expected to lead to deeper understanding of tribocharging, and consequently of aggregation and flow behaviour of many particle systems.

## Acknowledgements

We are thankful to Peter Jones, Tim Moore and Trevor Berry for technical assistance and Julian Phillips for building the Laser Flash Unit.

## Appendix A. Rotational drag force calculation

The angular momentum conservation of the particle is

$$J\frac{du_\theta}{dt} = (\vec{P}X\vec{E}) - G \tag{A.1}$$

where $u_\theta$ = angular velocity of the particle.

Drag torque $G$ for a sphere of radius $R_p$ is calculated as [14]

$$G = 8\pi\mu u_\theta R_p^3 \tag{A.2}$$

For a spherical shell as in the case of hollow glass bubbles, the moment of inertia

$$J = \frac{2}{3}mR_p^2 \tag{A.3}$$

where $m$ = mass of the shell.

The cross product $\vec{P}X\vec{E}$ in terms of its components can be calculated as

$$\vec{P}X\vec{E} = (P_zE_r - P_rE_z)i + (P_rE_y - P_yE_r)j + (P_yE_z - P_zE_y)k \tag{A.4}$$

It was assumed that the particle dipole alignment was perpendicular to the $r$–$z$ plane and parallel to the $y$ direction when it came out of the plates, so calculations were made for the dipole alignment during the trajectory flight using the three component equations to predict the rotation of dipole in all three directions.

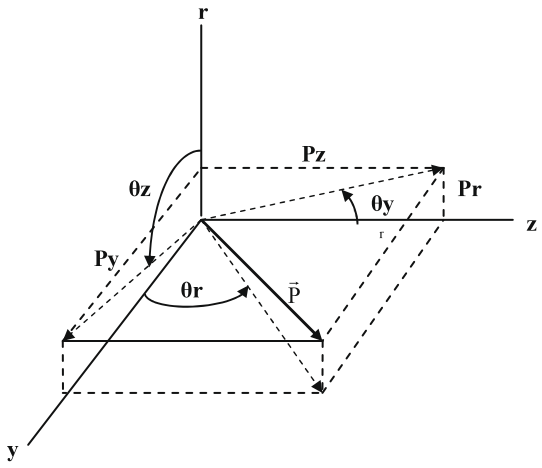


**Fig. A.1.** Angles between direction of vector $P$ and the co-ordinate axes.

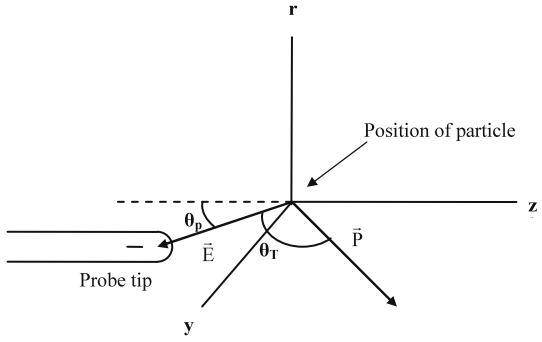


**Fig. A.2.** Dipole-to-field angle $\theta_T$. Note probe axis is in the $r$–$z$ plane.

The angular acceleration in the $r$ direction from Eq. (A.1) is

$$\frac{du_{\theta r}}{dt} = \frac{3}{2mr_p^2}\left((P_yE_z - P_zE_y) - 8\pi\mu r_p^3 u_{\theta r}\right) \tag{A.5}$$

Similar equations can be written for angular acceleration in the $z$ and $y$ directions. The angles $\theta_y, \theta_z, \theta_r$ calculated by integrating the gradients were then used to calculate components of vector P (Fig. A.1).

$$P_r = P_y/\tan\theta_z \tag{A.6}$$

$$P_z = P_y\tan\theta_r \tag{A.7}$$

$$P_y = \sqrt{\frac{P^2}{(1/\tan\theta_z)^2 + (\tan\theta_r)^2 + 1}} \tag{A.8}$$

The components of electric field in the $r$ and $z$ directions were calculated as

$$E_z = E\cos\theta_p, \quad E_r = E\sin\theta_p, \quad E_y = 0 \tag{A.9}$$

Using the dot product in Eq. (A.10) the angle between vector $P$ and $E$ was calculated. This angle, $\theta_T$ gives the direction of torque experienced by the dipole in the electric field.

$$\cos\theta_T = \frac{P.E}{|P||E|} \tag{A.10}$$

Calculations were made to predict the time required for $\theta_T$ to change from 90° (initial position) to 0° or 180° depending on whether the electric field direction was pointing away or towards the probe (probe positive or negative, respectively).

For example consider the 80 μm particle described in Fig. 6 with mass $4 \times 10^{-11}$ kg. The predicted dipole strength was

$P = 2.16 \times 10^{-17}$ C m. With an axial velocity of 2.75 m/s, the time taken to travel through the preselector plates was 55 ms. Assuming that before entering the plates the dipole was perpendicular to the electric field between the plates (towards negative $y$-axis), thus experiencing a repelling torque. Using the angular momentum equations the time taken by the dipole to orient 180° to the electric field i.e. towards positive $y$-axis was approximately 180 μs. Hence in comparison to the time spent between the plates it is safe to assume that the dipole on the particles leaving the plates is pointing along the positive $y$-axis. For the trajectory simulation, this orientation is assumed constant up to the point where the dipole is affected by the field gradient; in this case for $r_{sph} = 3611$ μm. The time taken after this for this dipole to rotate from 90° down to 15° misalignment with the electric field of probe was 340 μs.

## References


[1] W.M. Farrell, M.D. Desch, M.L. Kaiser, J. Houser, G.A. Landis, D.M. Wilt, Radio and optical detection of Martian dust storm discharges, Acta Astronaut. 46 (1) (2000) 25–36.

[2] D.J. Lacks, A. Levandovsky, Effect of particle size distribution on the polarity of triboelectric charging in granular insulator systems, J. Electrostat. 65 (2007) 107–112.

[3] J.R. Marshall, F. Freund, T. Sauke, M. Freund, Catastrophic collapse of particulate clouds: implications from aggregation experiments in the USML-1 and USML-2 glovebox. NASA TM 1998-208697, Second United States Microgravity Laboratory:One Year Report, vol. 2, 35/579-35/592, 1997.

[4] J.R. Marshall, T.B. Sauke, J.N. Cuzzi, Microgravity studies of aggregation in particulate clouds, Geophys. Res. Lett. 32 (2005) L11202.

[5] W. Balachandran, W. Machowski, E. Gaura, C. Hudson, Control of drug aerosol in human airways using electrostatic forces, J. Electrostat. 40&41 (1997) 579–584.

[6] J. Abrahamson, J. Marshall, Permanent electric dipoles on gas-suspended particles and the production of filamentary aggregates, J. Electrostat. 55 (2002) 43–63.

[7] J. Marshall, personal correspondence, 2005.

[8] G. Zebel, Coagulation of aerosols, in: C.N. Davies (Ed.), Aerosol Sci., Academic Press, New York, 1966, p. 31.

[9] H. Wang, R.C. Bell, M.J. Iedema, et al., Sticky ice grains aid planet formation: unusual properties of cryogenic water ice, Astrophys. J. 620 (2) (2005) 1027–1032. Part 1.

[10] F.F. Abraham, Functional dependence of drag coefficient of a sphere on Reynolds number, Phys. Fluids 13 (1970) 2194–2195.

[11] R.B. Bird, W.E. Stewart, E.N. Lightfoot, Transport Phenomena, John Wiley and Sons, 1962. pp. 57–58.

[12] Y.T.C. Ko, J.P. Huang, K.W. Yu, The dielectric behaviour of single-shell spherical cells with a dielectric anisotropy in the shell, J. Phys. Condens. Mat. 16 (2004) 499–509.

[13] I. Wygnanski, H. Fiedler, Some measurements in the self-preserving jet, J. Fluid Mech. 38 (1969) 577–612.

[14] G.B. Jeffrey, Steady rotation of a solid of revolution in a viscous fluid, Proc. London Math. Soc. (21) (1915) 327–338.